Spinel Structural Disorder Influences Solar Water Splitting Performance of $ZnFe_2O_4$ Nanorod Photoanodes

Xiaodi Zhu, Néstor Guijarro,* Yongpeng Liu, Pascal Schouwink, Rebekah A. Wells, Florian Le Formal, Song Sun, Chen Gao, Kevin Sivula*

X. Zhu, Dr. N. Guijarro, Y. Liu, R. A. Wells, Dr. F. Le Formal, Prof. K. Sivula
Laboratory for Molecular Engineering of Optoelectronic Nanomaterials (LIMNO), École Polytechnique Fédérale de Lausanne (EPFL), Station 6, 1015 Lausanne, Switzerland
E-mail: nestor.guijarro@epfl.ch, kevin.sivula@epfl.ch
X. Zhu, Dr. S. Sun, Prof. C. Gao
National Synchrotron Radiation Laboratory, University of Science and Technology of China, No.42, Hezuohua Road, Hefei, Anhui, 230029, P. R. China
Dr. P. Schouwink
Institute of Chemical Sciences and Engineering, École Polytechnique Fédérale de Lausanne, Rue de l'Industrie 17, 1951 Sion, Switzerland

Abstract: Zinc spinel ferrite, $ZnFe_2O_4$ (ZFO), is an emerging photoanode material for photoelectrochemical (PEC) solar fuel production. However, a lack of fundamental insight into the factors limiting the photocurrent has prevented substantial advance in the performance of ZFO. Herein we find that ZFO nanorod array photoelectrodes with varying crystallinity (prepared by altering the synthesis temperature) exhibit vastly different PEC properties. Using a sacrificial hole scavenger (H_2O_2), spatially-defined carrier generation, and electrochemical impedance spectroscopy, we show that ZFO with a relatively poor crystallinity but a higher spinel inversion degree (due to cation disorder) exhibits superior photogenerated charge separation efficiency and improved majority charge carrier transport compared to ZFO with higher crystallinity and a lower inversion degree. Conversely, the latter condition leads to better charge injection efficiency. Optimization of these factors, and the addition of a nickel-iron oxide co-catalyst overlayer, leads to a new benchmark solar photocurrent for ZFO of 1.0 mA cm^{-2} at 1.23 V vs. RHE and 1.7 mA cm^{-2} at 1.6 V vs. RHE. Importantly, the observed correlation between the cation disorder and the PEC performance represents a new insight into the factors important to the PEC performance of the spinel ferrites and suggests a path to further improvement.

Photoelectrochemical (PEC) water splitting is a promising route for the scalable and cost-effective storage of solar energy and chemical fuel production, which are critical for a sustainable, carbon-neutral, and global energy economy.[1] While impressive solar-to-hydrogen conversion efficiency using PEC devices has been demonstrated[2,3] the development of low-cost and robust photoelectrode materials that deliver high-performance while also tolerating the harsh PEC operating conditions is still required.[4] In this regard, the semiconducting metal oxides[5] are promising photoanode materials due to their excellent durability and relative low cost. Despite the intense development of many metal oxides (*e.g.* Fe_2O_3,[6] WO_3,[7,8] and $BiVO_4$[9]), the identification of a suitable photoanode material remains a challenge. However, given the vast number of possible ternary and multinary metal oxides, interest in developing an ideal material remains.[10]

The spinel ferrites (*M*Fe_2O_4, *M* = Zn, Mg, Cu, Ca, etc.) represent an attractive class of ternary metal oxides as photoelectrodes for PEC solar water splitting[4,10] given their suitable light harvesting in the visible range (band gap energy, $E_g = 1.4 \sim 2.1$ eV), abundant constituent elements, and demonstrated long-term photo-stability.[11,12] Specifically, n-type $ZnFe_2O_4$ (ZFO) has garnered considerable interest as a secondary overlayer component of various composite photoelectrode systems such as TiO_2/ZFO,[13,14] Fe_2O_3/ZFO,[15,16] and ZnO/ZFO,[17] to enhance photogenerated charge extraction in the primary oxide. However, as the main active photoanode material for PEC water oxidation, the performance of ZFO has remained relatively modest despite the various improvement strategies employed. Specifically, ZFO photoanodes have been prepared via aerosol-assisted chemical vapor deposition giving nanostructured films,[18,19] using atomic layer deposition on a nanostructured scaffold,[20] and with spray pyrolysis with metal-doping,[21] but the solar photocurrent densities for water oxidation have remained on the order of 100 μA cm^{-2}. Recently, Kim *et al*. reported an innovative route to fabricate ZFO using a β-FeOOH nanorod array precursor.[22,23] The resulting ZFO nanorod films were further

improved via hydrogenation and a microwave annealing treatment to advance the observed solar water oxidization photocurrent density to 0.35 mA cm^{-2} at 1.23 V vs. RHE (the reversible hydrogen electrode). However, this is still far below the theoretical maximum value of ca. 11 mA cm^{-2} with ZFO. Thus to further advance the PEC performance of ZFO, it is essential to identify the key material characteristics which govern its performance. Herein, we report the importance of the structural disorder on the charge transport and transfer in ZFO photoanodes. Our results suggest that the spinel inversion degree is a critical parameter influencing the PEC performance of spinel ferrite photoelectrodes. The further optimization of these electrodes leads to a new benchmark photocurrent for solar water oxidation with ZFO.

Nanorod-array ZFO photoanodes were prepared using a modified conversion route[12] via β-FeOOH on F-doped tin oxide (FTO) coated glass substrates (full experimental details described in the Supporting Information, SI). The synthesis was performed at 500 °C, 600 °C, 700 °C or 800 °C (for 20 min, which was sufficient to form the spinel and avoided adversely affecting the electrical resistivity of the FTO substrate, see Table S1, SI) and a final annealing at 200 °C under H$_2$ was added to increase the n-type character. The resulting photoelectrodes are denoted as ZFO-500, ZFO-600, ZFO-700, and ZFO-800, respectively. The morphology of the β-FeOOH precursor and the resulting ZFO nanorod arrays are shown by scanning electron micrograph (SEM) images in **Figure 1**. A similar morphology consisting of nearly vertically-oriented nanorods *ca*. 500 nm in length is observed in all cases indicating that the synthesis temperature did not significantly affect the ZFO nanorod array structure. Importantly, the diameter of the nanorods for all temperatures is *ca*. 45 nm. Analysis by X-ray photoelectron spectroscopy (XPS) did not evidence any obvious surface composition difference and furthermore confirmed similar oxidation states among samples (see Figure S1, SI). Specifically, the mid-binding-energy O 1s signal at 531.8 eV attributed to O^{2-} in oxygen deficient regions remains constant (relative integrated value of 17-18%) indicating that the H$_2$ treatment had a

similar effect on the concentration of oxygen vacancies irrespective of the synthesis temperature. In addition, the UV-Vis absorption spectra (See Figure S2, SI) shows no trend in the light absorption of the ZFO photoelectrodes with synthesis temperature. An indirect E_g of 1.9 eV and a direct E_g of 2.1 eV were estimated for all samples, however it is important to mention that light absorption by the indirect transition does not effectively drive PEC processes in these materials.[24]

Despite the seemingly identical properties of the ZFO prepared at different temperatures as observed by SEM, XPS, and UV-Vis, differences in crystallinity were observed by thin-film X-ray diffraction (XRD, **Figure 2**a) where the intensity of the peaks corresponding to the (220), (311), and (511) reflections strengthened as the synthesis temperature increased. Powder XRD (PXRD) performed on ZFO synthesized by the same procedure without FTO substrates gave the same trend (See Figure S3, SI) and allowed the detailed structural analysis by Rietveld refinement, which further revealed trends in the estimated domain size and the distribution of cations with the synthesis temperature. As shown in the inset to Figure 2a (circle markers), the crystalline domain size, d, (estimated by the integral breadth) increases as the synthesis temperature increases. It should be noted that the value of d assumes an isotropic domain shape, which is an approximation in the case of our nanorod-shaped features, however, the trend of increasing domain size with temperature is expected. More importantly, the spinel inversion degree (δ) decreases from 0.30 to 0.13 when the synthesis temperature increased from 500 °C to 800 °C (see Figure 2a inset, square markers), consistent with other reports.[25–28] Since the spinel crystal structure is composed of a cubic closed-packed array of oxygen atoms with the tetrahedral and octahedral cavities occupied by divalent or trivalent cations, the structural formula of zinc ferrite can be written as $Fe_\delta^T Zn_{1-\delta}^T Zn_\delta^O Fe_{2-\delta}^O O_4$ where the superscripts T and O denote tetrahedral and octahedral sites, respectively, and δ represents the inversion degree (which is a metric of cation disorder and defined by the fraction of the T sites occupied by Fe^{3+}).

The crystallographic structure of ZFO with varying δ is illustrated in Figure 2b. In prototypical ZFO ($\delta = 0$), Zn^{2+} and Fe^{3+} occupy T and O sites, respectively, while in completely inverted ZFO ($\delta = 1$), T sites are occupied by Fe^{3+} and the O sites are equally occupied by Zn^{2+} and Fe^{3+}. The completely random distribution of Zn^{2+} and Fe^{3+} corresponds to $\delta = 0.67$.[29]

To investigate how the observed structural changes affect photoanode performance, current density-potential characteristics (J-V curves) were measured under standard conditions (1 M NaOH electrolyte, intermittent 1 Sun illumination). We note that the J-V behavior was reproducible, stable, and the photocurrent magnitude was verified by integrating the incident-photon-to-current (IPCE) spectra (see Figure S4, SI). Additionally, a Faradaic efficiency of ca. 99% for O_2 production has been measured on our ZFO to confirm that the photocurrent results from solar water oxidation.[12] Typical results for photoanodes prepared at the different synthesis temperatures are shown in **Figure 3**a. Remarkably, the performance is strongly influenced by the synthesis temperature. ZFO-600 delivers the highest photocurrent density, J_{photo}, surpassing 0.8 mA cm^{-2} at 1.23 V and rising to 1.7 mA cm^{-2} at 1.6 V vs. RHE. While ZFO-800 exhibited the most favorable photocurrent onset potential (at ca. 0.8 V vs. RHE), J_{photo} remained below 1.0 mA cm^{-2}. In contrast, ZFO-500 exhibited a more positive onset potential (ca. 1.2 V vs RHE) but J_{photo} was higher than ZFO-800 at high applied potential.

Further insight into the significantly different PEC performance was sought by employing H_2O_2 as a hole scavenger. The corresponding J-V curves (Figure S5, SI) were used to estimate the photogenerated charge separation efficiency, η_{sep}, and minority charge carrier injection efficiency, η_{inj}.[30] Indeed, the water oxidation photocurrent density can be described as $J_{photo} = J_{abs} \eta_{sep} \eta_{inj}$ where J_{abs} is the theoretical maximum photocurrent density considering the measured light absorption (J_{abs} is estimated to be 7.5 mA cm^{-2}, see SI for calculation details). Figure 3b shows η_{sep} and η_{inj} as a function of the applied potential. The values of η_{inj} increase abruptly at a potential matching well with the photocurrent onset potential and reach close to

90% at 1.4 V vs RHE, except for ZFO-500 which only reaches 20%. The distinct behavior of ZFO-500 could tentatively be attributed to the nanorod surface, which likely contains a higher concentration of surface traps. Indeed, a slight evolution of the nanorod tip morphology from sharp facets to smooth and rounded can be seen by careful comparison of the SEM images for ZFO-500 (Figure 1c) and ZFO-800 (Figure 1f), which we suggest to be related to surface defect states. High resolution transmission electron microscopy (HRTEM) data was also acquired on nanorods removed from ZFO-500 and ZFO-800 samples (See Figure S6, SI). Generally, the difference in morphology observed by SEM and implied with the crystallite size from XRD are consistent with the TEM measurements, in addition lattice fringes are observable for both samples up to the surface of the nanorods. This suggests that no obvious amorphous surface layer is present that could be acting as surface traps. However, we cannot discount the presence of surface defects in the first atomic layers. Indeed, we note that the observed evolution of the photocurrent onset potential to more favorable values has been explained by the repair of surface defects in similar systems.[31] Regardless of the presence of surface traps in the 500°C sample, at sufficiently high applied potential recombination at surface traps does not limit the photocurrent in the 600°C-800°C ZFO photoanodes as η_{inj} approaches unity.

On the other hand, the value of η_{sep} for all samples never rises above 35%, thus understanding its behavior is essential. Interestingly, η_{sep} decreases systematically with increasing synthesis temperature. The striking difference between η_{sep} in ZFO-500 and ZFO-800 (*i.e.* 35% and 9%, respectively, at 1.4 V vs RHE) and the absence of a clear morphological explanation suggest that differences in charge carrier transport/recombination in the bulk of the material are responsible. More precisely, in nanorod-array photoelectrodes photogenerated majority charge carriers (electrons for a n-type photoanode) travel the axial length of the nanorod to the collecting substrate while minority charge carriers (holes in this case) travel the relatively shorter radial distance to the semiconductor liquid junction (SCLJ). A change in either

6

of these transport processes will alter the photogenerated carrier recombination rate, and result in different measured η_{sep}. Conveniently, the limiting transport process in nanorod arrays can be resolved by spatially confining the zone of carrier generation.[32]

Since the estimated penetration depth of 2.74 eV photons ($\lambda = 452$ nm) in our ZFO nanorods is *ca*. 200 nm (see SI for calculation) compared to the nanorod length of 500 nm, using substrate-side illumination (SSI) or electrolyte-side illumination (ESI) with monochromatic photons ($\lambda = 452$ nm) generates charge carriers in different zones of the nanorods as depicted in **Figure 4**a. The ratio of the measured photocurrents using ESI and SSI, *i.e.* J_{ESI}/J_{SSI}, is shown in Figure 4b for ZFO-500 and ZFO-800 (see J-V curves in Figure S7, SI). If majority carrier transport does not limit the photocurrent, $J_{ESI}/J_{SSI} = 1$ is expected. Interestingly, both ZFO-500 and ZFO-800 show values far from 1 when measured in standard 1 M NaOH electrolyte (open markers Figure 4b). For ZFO-800, $J_{ESI}/J_{SSI} = 0.5$, suggesting that majority carrier transport limits η_{sep} in this case (more majority carriers are collected when they are generated close to the substrate).

In stark contrast, ZFO-500 gives a J_{ESI}/J_{SSI} of 1.5. While this shows that majority carrier transport does not limit η_{sep} in ZFO-500, it could further indicate that minority carrier transport is more efficient (less recombination occurs) when charges are generated at the nanorod tips. However, in 1 M NaOH electrolyte the slow kinetics of the water oxidation reaction cannot be discounted, as minority carriers can accumulate at the SCLJ. To eliminate any effects due to a kinetic bottleneck, J_{ESI}/J_{SSI} was also measured in sacrificial H_2O_2 electrolyte. In this case (Figure 4b, filled markers), ZFO-500 gives the expected $J_{ESI}/J_{SSI} = 1$, confirming that majority carrier transport does not limit η_{sep}. Conversely, J_{ESI}/J_{SSI} remains at 0.5 for ZFO-800, verifying the limitation in majority carrier transport. In addition, the trend with J_{ESI}/J_{SSI} was observed to be independent of the illumination intensity (with $\lambda = 452$ nm), but when $\lambda = 525$ nm (and the estimated penetration depth is *ca*. 500 nm) $J_{ESI}/J_{SSI} = 1$ in all cases as expected (See Figure S7).

The deduction that the majority carrier transport differs significantly between ZFO-500 and ZFO-800 was further verified by extracting the bulk resistance (R) from electrochemical impedance spectroscopy (EIS) in H_2O_2 under illumination (see Nyquist and Bode plots Figure S8, SI). As shown in Figure 4c, R is observed to be approximately a factor of 5-10 greater for ZFO-800 over a broad potential range. To better support the change in the electronic properties of the ZFO prepared at different temperatures the conductivity of the ZFO-500 and ZFO-800 nanorod arrays were directly measured (see Figure S9 and Calculation Note S3, SI). The results are consistent with a higher conductivity of the ZFO-500 sample. Indeed, the estimated values are 89.1 µS/cm and 12.4 µS/cm for the ZFO-500 and ZFO-800 sample, respectively.

The detailed PEC analysis of ZFO-500 and ZFO-800 provide a convincing explanation as to the performance of ZFO as a function of synthesis temperature. At low synthesis temperatures, ZFO electrodes exhibit good charge transport characteristics but a limitation of photogenerated carrier recombination at the SCLJ. In contrast at high synthesis temperatures, the efficient charge injection for the water oxidation reaction occurs at the SCLJ, but poor majority charge carrier transport limits the performance. The optimization of these opposing factors leads to the best performance at a synthesis temperature of 600 °C. It is important to note that the poor SCLJ properties of the ZFO-500 sample can be somewhat overcome by adding a co-catalyst (*e.g.* nickel-iron oxide[33]), which shifts the onset of photocurrent by *ca.* 100 mV, but its performance remains below that of ZFO-600 (See Figure S10, SI). This further indicates that surface trapping states are positioned at energies insufficient to drive water oxidation in ZFO-500.[34] In contrast, no beneficial effect of adding a co-catalyst on ZFO-800 is observed, as expected from its superior η_{inj}. The addition of a nickel-iron oxide co-catalyst on the optimized ZFO-600 modestly shifts the onset potential by 50 mV and leads to a J_{photo} of 1.0 mA cm^{-2} at 1.23 V vs RHE (Figure S10).

Regarding the relationship between the PEC performance and the crystallinity of the ZFO, the apparent decrease in charge carrier transport efficiency with increasing synthesis temperature is surprising, as higher crystallinity (larger d) is generally expected to enhance semiconductor transport properties.[35] However, the aforementioned correlation between the synthesis temperature and the crystal structure rather suggests that more cation disorder (higher δ) is linked to the superior charge transport. This conclusion can be rationalized by the expected changes in electronic structure during the normal-inverse spinel transition. While four-coordinated Fe^{3+} (ionic radius of 0.63 Å) and of Zn^{2+} (0.60 Å) have similar sizes (causing little crystallographic distortion when Fe^{3+} occupies a T site), the difference in size of six-coordinated Zn^{2+} (0.74 Å) compared to Fe^{3+} (0.65 Å) indicates a substantial distortion when Zn^{2+} occupies an O site.[28,36] Besides, cation disorder induces magnetic changes such as introducing an Fe^T-O-Fe^O superexchange interaction.[37–39] These factors contribute to changes in the electronic structure that have been recently predicted in first-principles calculations by Sun et al.[40] where narrower electronic bands near the Fermi level of ZFO were found with disordered cations compared to the prototypical structure. Computational studies and conductivity measurements on other spinel oxides including $SnFe_2O_4$, $ZnCo_2O_4$ and $NiCo_2O_4$ have also recently indicated a more metallic conductivity with increasing δ[41,42] consistent with our experimental results (Figure S9). Thus, we suggest that the electronic structure arising from cation disorder in ZFO could aid charge transport via a hopping mechanism, as the conductivity of ZFO is likely based on small polaron hopping.[43] While the results presented here are consistent with a clear link between cation disorder, the majority carrier transport, and the PEC performance of ZFO photoanodes, the complex effects of cation disorder and crystallinity on the lifetime and transport of minority carriers and the role of defect states in the bulk, at grain boundaries, and at the SCLJ in ZFO remain points of interest to further advance the charge separation efficiency.

In summary, a new benchmark in the performance of $ZnFe_2O_4$ (ZFO) photoanodes for solar water oxidation has been achieved using nanorod arrays and by balancing the efficiencies for photogenerated charge separation and injection. Adding a nickel-iron oxide co-catalyst overlayer on optimized ZFO photoanodes gave solar photocurrents of up to 1.0 mA cm^{-2} at 1.23 V vs RHE and 1.7 mA cm^{-2} at 1.6 V vs. RHE. Although modifying the ZFO synthesis temperature did not change the optical properties or the diameter of the nanorods, we found temperature to affect the crystallinity and cation disorder in the spinel structure, and this was strongly linked to the bulk charge separation and injection properties. Interestingly, ZFO with a relatively poor crystallinity but a high degree of cation disorder was found to exhibit superior photogenerated charge separation efficiency and promoted majority charge carrier transport compared to ZFO with higher crystallinity and low cation disorder. This suggests for the first time, that the degree of cation disorder could be an important factor in the PEC performance of ZFO. The further understanding and control of this aspect in spinel ferrites will likely advance the performance in this class of promising materials. Moreover, the solution-based and facile fabrication used to prepare the optimized ZFO nanorod photoanodes makes this system a promising candidate for inexpensive large-area storage of solar energy via PEC water splitting.

References

[1] N. S. Lewis, *Science* **2016**, *351*, aad1920.
[2] J. L. Young, M. A. Steiner, H. Döscher, R. M. France, J. A. Turner, T. G. Deutsch, *Nat. Energy* **2017**, *2*, 17028.
[3] J. W. Ager, M. R. Shaner, K. A. Walczak, I. D. Sharp, S. Ardo, *Energy Environ. Sci.* **2015**, *8*, 2811.

[4] K. Sivula, R. van de Krol, *Nat. Rev. Mater.* **2016**, 16010.

[5] Y. Yang, S. Niu, D. Han, T. Liu, G. Wang, Y. Li, *Adv. Energy Mater.* **2017**, *7*, 1700555.

[6] K. Sivula, F. Le Formal, M. Grätzel, *ChemSusChem* **2011**, *4*, 432.

[7] T. Zhu, M. N. Chong, E. S. Chan, *ChemSusChem* **2014**, *7*, 2974.

[8] C. A. Bignozzi, S. Caramori, V. Cristino, R. Argazzi, L. Meda, A. Tacca, *Chem. Soc. Rev.* **2013**, *42*, 2228.

[9] H. L. Tan, R. Amal, Y. H. Ng, *J. Mater. Chem. A* **2017**, *5*, 16498.

[10] F. F. Abdi, S. P. Berglund, *J. Phys. Appl. Phys.* **2017**, *50*, 193002.

[11] L. G. J. de Haart, G. Blasse, *J. Electrochem. Soc.* **1985**, *132*, 2933.

[12] N. Guijarro, P. Bornoz, M. Prévot, X. Yu, X. Zhu, M. Johnson, X. Jeanbourquin, F. L. Formal, K. Sivula, *Sustain. Energy Fuels* **2018**, *2*, 103.

[13] X.-L. Zheng, C.-T. Dinh, F. P. G. de Arquer, B. Zhang, M. Liu, O. Voznyy, Y.-Y. Li, G. Knight, S. Hoogland, Z.-H. Lu, X.-W. Du, E. H. Sargent, *Small* **2016**, *12*, 3181.

[14] Y. Hou, X.-Y. Li, Q.-D. Zhao, X. Quan, G.-H. Chen, *Adv. Funct. Mater.* **2010**, *20*, 2165.

[15] K. J. McDonald, K.-S. Choi, *Chem. Mater.* **2011**, *23*, 4863.

[16] Y. Guo, Y. Fu, Y. Liu, S. Shen, *RSC Adv.* **2014**, *4*, 36967.

[17] A. Sheikh, A. Yengantiwar, M. Deo, S. Kelkar, S. Ogale, *Small* **2013**, *9*, 2091.

[18] A. A. Tahir, K. G. U. Wijayantha, *J. Photochem. Photobiol. Chem.* **2010**, *216*, 119.

[19] A. A. Tahir, H. A. Burch, K. G. U. Wijayantha, B. G. Pollet, *Int. J. Hydrog. Energy* **2013**, *38*, 4315.

[20] A. G. Hufnagel, K. Peters, A. Müller, C. Scheu, D. Fattakhova-Rohlfing, T. Bein, *Adv. Funct. Mater.* **2016**, *26*, 4435.

[21] Y. Guo, N. Zhang, X. Wang, Q. Qian, S. Zhang, Z. Li, Z. Zou, *J. Mater. Chem. A* **2017**, *5*, 7571.

[22] J. H. Kim, Y. J. Jang, J. H. Kim, J.-W. Jang, S. H. Choi, J. S. Lee, *Nanoscale* **2015**, *7*, 19144.

[23] J. H. Kim, J. H. Kim, J.-W. Jang, J. Y. Kim, S. H. Choi, G. Magesh, J. Lee, J. S. Lee, *Adv. Energy Mater.* **2015**, *5*, 1401933.

[24] S. Ida, K. Yamada, T. Matsunaga, H. Hagiwara, Y. Matsumoto, T. Ishihara, *J. Am. Chem. Soc.* **2010**, *132*, 17343.

[25] Q.-M. Wei, J.-B. Li, Y.-J. Chen, *J. Mater. Sci.* **2001**, *36*, 5115.

[26] S. Bid, S. K. Pradhan, *Mater. Chem. Phys.* **2003**, *82*, 27.

[27] C. N. C. J-M Greneche, *J. Phys. Condens. Matter.* **2000**, *12*, 7795.

[28] F. Bræstrup, B. C. Hauback, K. K. Hansen, *J. Solid State Chem.* **2008**, *181*, 2364.

[29] R. O. Sack, M. S. Ghiorso, *Contrib. Mineral. Petrol.* **1991**, *106*, 474.

[30] H. Dotan, K. Sivula, M. Grätzel, A. Rothschild, S. C. Warren, *Energy Environ. Sci.* **2011**, *4*, 958.

[31] J.-W. Jang, C. Du, Y. Ye, Y. Lin, X. Yao, J. Thorne, E. Liu, G. McMahon, J. Zhu, A. Javey, J. Guo, D. Wang, *Nat. Commun.* **2015**, *6*, 7447.

[32] P. Saurabh Bassi, L. Xianglin, Y. Fang, J. S. Chye Loo, J. Barber, L. Helena Wong, *Phys. Chem. Chem. Phys.* **2016**, *18*, 30370.

[33] R. D. L. Smith, M. S. Prévot, R. D. Fagan, Z. Zhang, P. A. Sedach, M. K. J. Siu, S. Trudel, C. P. Berlinguette, *Science* **2013**, *340*, 60.

[34] H. Hajibabaei, A. R. Schon, T. W. Hamann, *Chem. Mater.* **2017**, *29*, 6674.

[35] S. C. Warren, K. Voïtchovsky, H. Dotan, C. M. Leroy, M. Cornuz, F. Stellacci, C. Hébert, A. Rothschild, M. Grätzel, *Nat. Mater.* **2013**, *12*, 842.

[36] C. Klein, C. S. Hurlbut, J. D. Dana, *Manual of Mineralogy (after James D. Dana)*, New York Wiley, **1985**.

[37] T. Kamiyama, K. Haneda, T. Sato, S. Ikeda, H. Asano, *Solid State Commun.* **1992**, *81*, 563.

[38] V. Šepelák, K. Tkáčová, V. V. Boldyrev, S. Wiβmann, K. D. Becker, *Phys. B Condens. Matter* **1997**, *234–236*, 617.

[39] F. K. Lotgering, *J. Phys. Chem. Solids* **1966**, *27*, 139.

[40] D. Sun, M. X. Wang, Z. H. Zhang, H. L. Tao, M. He, B. Song, Q. Li, *Solid State Commun.* **2015**, *223*, 12.

[41] O. Mounkachi, M. Hamedoun, A. Benyoussef, *J. Supercond. Nov. Magn.* **2017**, *30*, 3035.

[42] P. F. Ndione, Y. Shi, V. Stevanovic, S. Lany, A. Zakutayev, P. A. Parilla, J. D. Perkins, J. J. Berry, D. S. Ginley, M. F. Toney, *Adv. Funct. Mater.* **2014**, *24*, 610.

[43] S. Boumaza, A. Boudjemaa, A. Bouguelia, R. Bouarab, M. Trari, *Appl. Energy* **2010**, *87*, 2230.
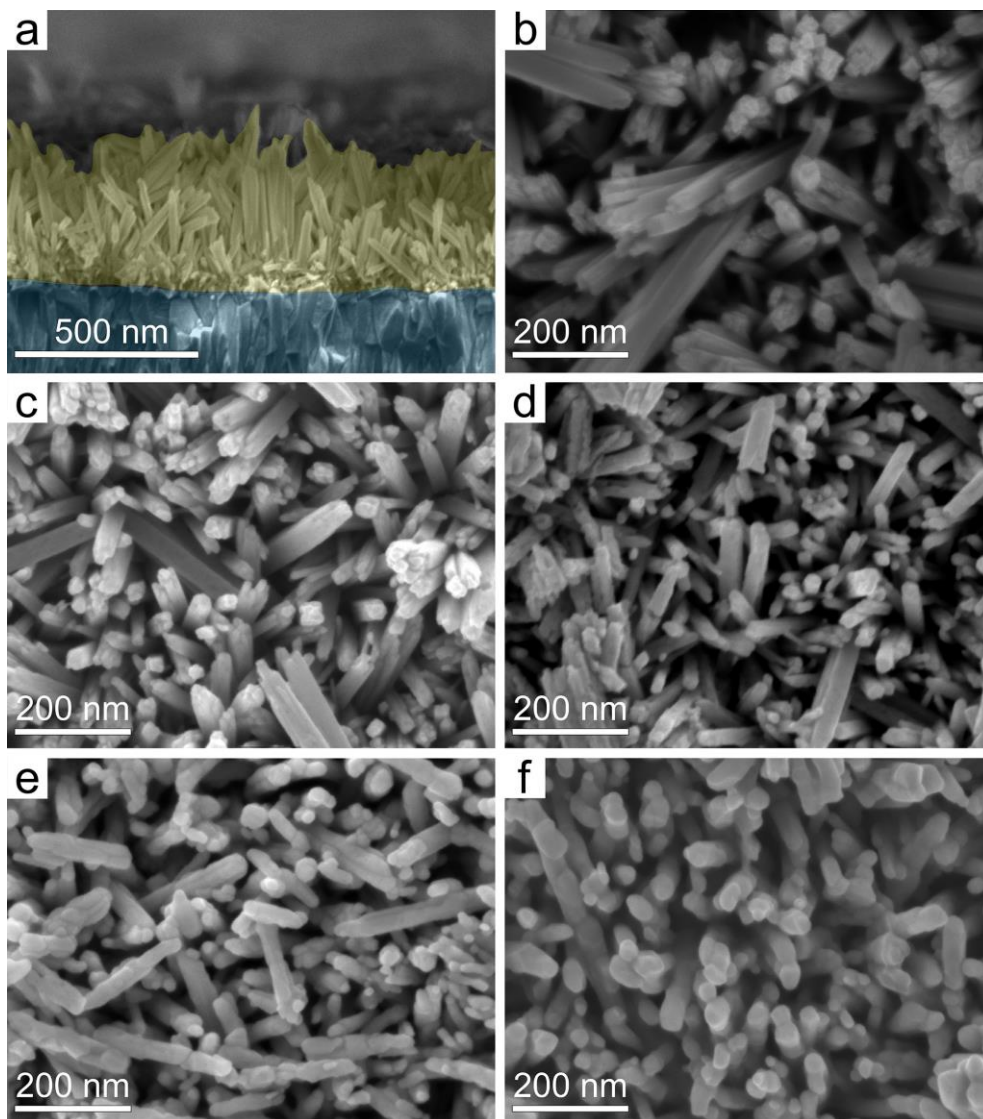
Figure 1. Scanning electron micrographs of (a,b) the β-FeOOH nanorod array precursor films (cross-section and top-down views, respectively). The FTO substrate is shaded blue in (a). Top-down images are also shown for (c) ZFO-500, (d) ZFO-600, (e) ZFO-700, and (f) ZFO-800.
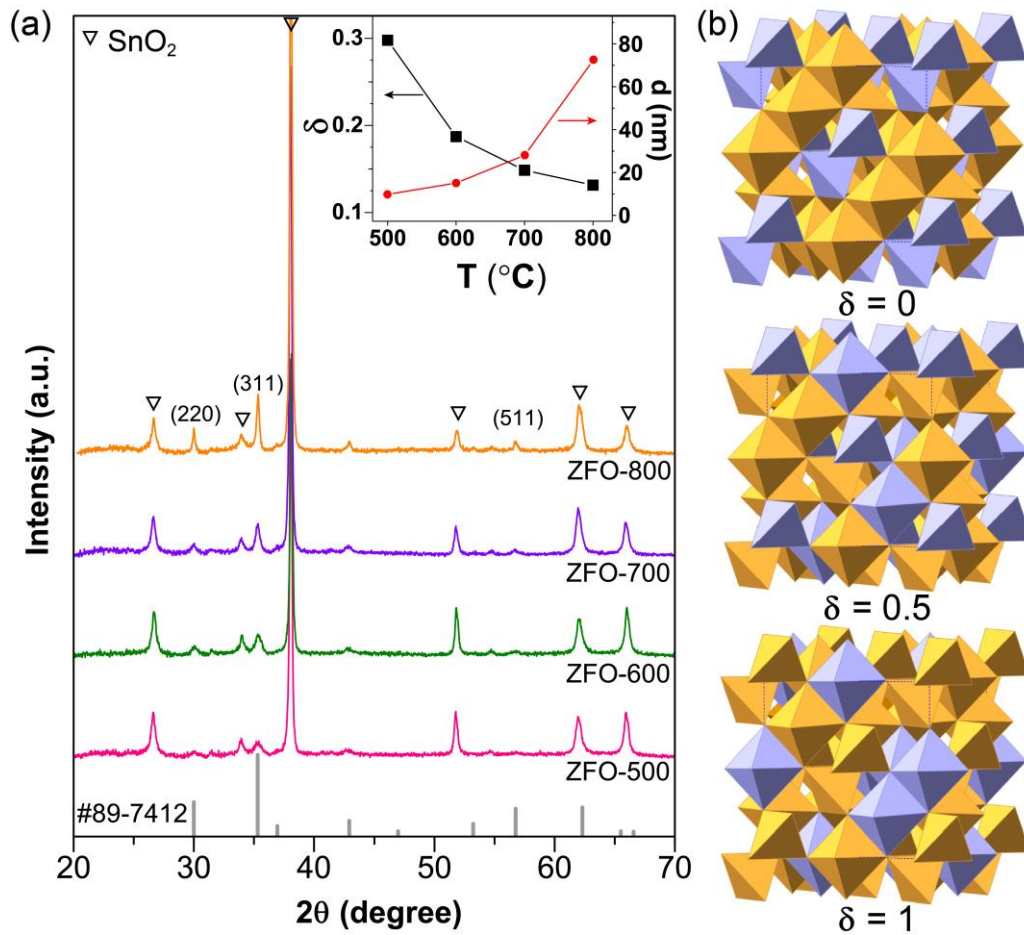
Figure 2. (a) XRD patterns of ZFO nanorod array photoelectrodes prepared on FTO coated glass are shown with the reference pattern for ZFO. The inset shows the spinel inversion degree, δ (square markers, extracted from the Rietveld refinement of PXRD data), and the estimated crystalline domain size, *d*, (circle markers) with respect to the ZFO synthesis temperature. (b) Crystallographic structures of the prototypical zinc ferrite spinel, partially inverted and totally inverted zinc ferrite spinel (yellow and purple polyhedrons are occupied by Fe^{3+} and Zn^{2+}, respectively).
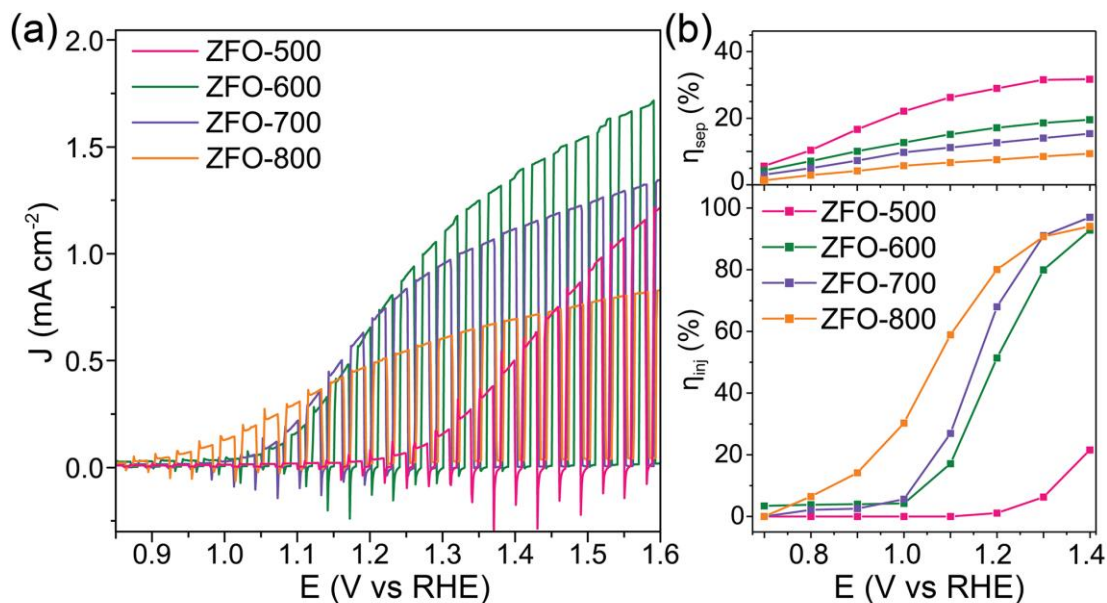
Figure 3. PEC performance of ZFO photoanodes. (a) Linear scanning J-V curves in 1M NaOH under intermittent 1 Sun illumination (100 mW cm^{-2}). (b) Estimated charge separation efficiency, η_{sep}, and minority charge carrier injection efficiency, η_{inj}.
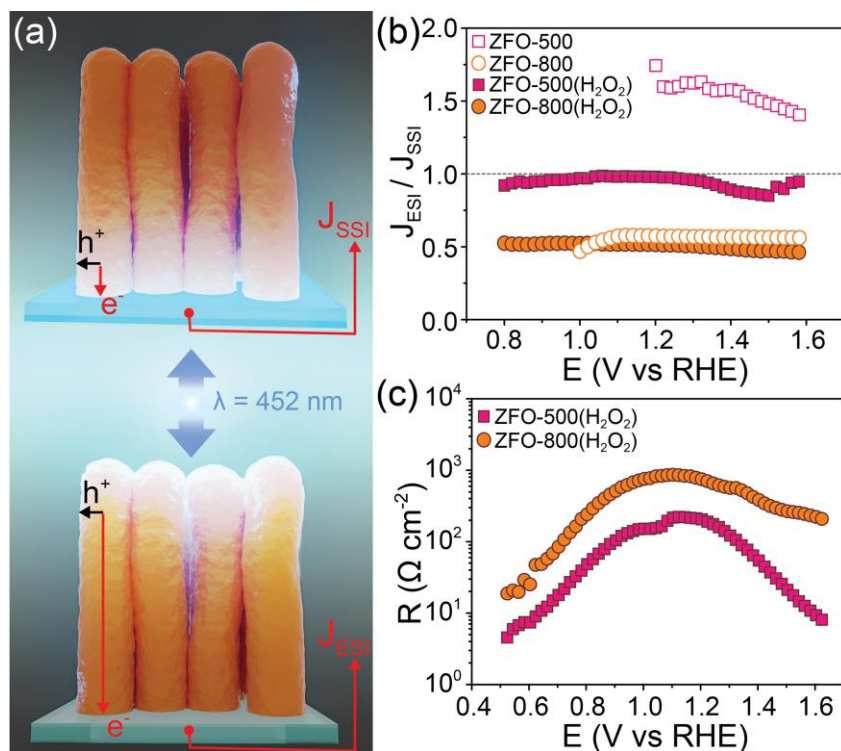

Figure 4. (a) Illustration of monochromatic substrate-side illumination (SSI, top) and electrolyte-side illumination (ESI, bottom) used to generate carriers principally in the base of the nanorods (SSI) or near the nanorod tips (ESI). (b) Ratio of ESI/SSI photocurrent density as a function of applied potential for the ZFO-500 and ZFO-800 in 1M NaOH (open markers) and in 1M NaOH + 0.5 M H$_2$O$_2$ (filled markers) (c) The semiconductor resistance extracted from EIS data measured in 1M NaOH + 0.5 M H$_2$O$_2$ under illumination.

15

Inverting the cations in the spinel structure of $ZnFe_2O_4$ is correlated to improved charge transport but poor surface properties. Optimization of these factors leads to benchmark performance in this ternary metal oxide for solar water oxidation.

Solar Fuel Production

X. Zhu, N. Guijarro,* Y. Liu, P. Schouwink, F. Le Formal, S. Sun, C. Gao, K. Sivula*

Spinel Structural Disorder Influences Solar Water Splitting Performance of $ZnFe_2O_4$ Nanorod Photoanodes
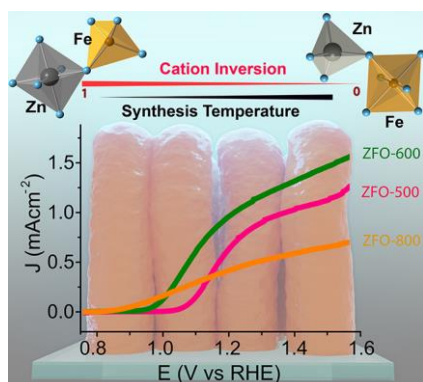
Supporting Information

Spinel Structural Disorder Influences Solar Water Splitting Performance of ZnFe$_2$O$_4$ Nanorod Photoanodes

Xiaodi Zhu, Néstor Guijarro,* Yongpeng Liu, Pascal Schouwink, Florian Le Formal, Song Sun, Chen Gao, Kevin Sivula*

Experimental details:

Fabrication of nanostructured zinc ferrite. First, arrays of iron oxyhydroxide (β-FeOOH) nanorods were fabricated on precleaned (acetone, ethanol and deionized water) FTO substrates (Solaronix TCO10-10) using a chemical bath deposition method[S1] with an aqueous bath (0.15 M FeCl$_3$, 1 M NaNO$_3$) at 100 °C for 3 h. The rinsed and dried β-FeOOH nanorod arrays were then coated with excess zinc nitrate (drop casting from aqueous solution onto the hot, 100°C substrate) and subsequently transferred to a tubular furnace already heated to 500 °C, 600 °C, 700 °C or 800 °C, for 20 min followed by natural cooling (leaving the samples in the furnace to cool slowly to room-temp, ca. 8 h). It should be noted that this is in contrast to our previous quick-cooling method.[12] The as-obtained samples were immersed in concentrated NaOH solution overnight to remove the ZnO overlayer. Afterwards, a hydrogenation procedure at 200 °C for 60 min was applied to finish the fabrication. Select samples were additionally coated with a nickel-iron oxide co-catalyst overlayer as previously described.[S2] Powder samples were obtained by mechanically mixing excess solid zinc nitrate with β-FeOOH obtained from the chemical bath after deposition in the FTO. Solid state mixtures were subject to the same heat treatment and H$_2$ annealing as the thin film samples.

General material characterization. X-ray diffraction patterns (XRD) of thin film samples were recorded on an Empyrean (PANalytical) diffractometer in Bragg-Brentano geometry. Powder X-ray diffraction (PXRD) was conducted on a Bruker D8 Discover diffractometer using a non-monochromatized Cu-source, a Nickel filter and a LYNXEYE-XE energy-dispersive detector, which was set to filter Fe-fluorescence. Experiments were performed in both Bragg-Brentano (low background Si sample holder) and Debye-Scherrer (0.8 mm borosilicate capillary) geometry, while spinning the sample. The transmission (DS) measurement was performed as a cross-check, and allowed excluding possible orientational effects owed to crystallite morphology, which could prevent Rietveld analysis of cation disorder, as they also influence Bragg intensities. Results presented were extracted from Rietveld refinements on samples measured in reflection, due to superior intensities and resolution. Rietveld analysis was done using Topas[S3] in Launch mode. Along with the scale factor and lattice parameter, 5 structural parameters were refined, being the inversion degree (coupling occupancies of Fe and Zn on T and O sites), one parameter x for the atomic position of the oxygen atom (Wyckoff site 32e, x,x,x) and one isotropic displacement parameter for each atom type. The background was modelled with a Chebyshev polynomial, peak profiles were modelled with a Pearson VII function (Rietveld fits in Fig. S3). Scanning electron microscopy (SEM) images were collected on a Zeiss Merlin microscope with an acceleration voltage of 3 keV, 79 pA probe current, using

an in-lens detector with a working distance of 3 mm. TEM and High-resolution TEM for the 800 C samples were measured using a Technai Osiris or an FEI Talos electron microscope operated at 200 kV. Samples for TEM measurement were prepared by scraping off nanorods on to a holey carbon support grid. High resolution XPS spectra were acquired using a KRATOS AXIS ULTRA spectrometer (Al Kα source, 600×750 μm spot size). Absorption spectra were recorded on a UV-vis-NIR UV-3600 (Shimadzu) spectrophotometer equipped with an integrating sphere.

Photoelectrochemical measurements. A potentiostat (BioLogic SP-200) and a Capuccino-type PEC cell were employed with a Ag/AgCl (saturated KCl) reference electrode and a Pt wire counter electrode. An active working electrode geometric area (0.238 cm^2) was defined. Simulated solar illumination was provided from a filtered 450 W Xenon-arc lamp (Muller Elektronik), calibrated to provide 1 Sun illumination (AM 1.5G, 100 mW cm^{-2}). For SEI/ESI experiments monochromatic illumination (@452 nm or 525 nm) was provided from an array of RGBW Star LEDs (Cree). Chopped-light linear sweep voltammograms were typically recorded from −0.5 V to +0.6 V versus Ag/AgCl with a scan rate of 10 mV s^{-1} in 1 M NaOH or 1 M NaOH + 0.5 M H$_2$O$_2$ electrolyte. Electrochemical impedance spectra (EIS) were acquired in 1 M NaOH + 0.5 M H$_2$O$_2$ under 1 Sun illumination in the AC potential frequency range of 1 MHz-0.1 Hz with an amplitude of 10 mV. Incident photon to current efficiency (IPCE) was estimated using a Tunable PowerArc illuminator (Optical Building Block Corporation) calibrated with a S120VC Photodiode Power sensor (Thorlabs). Chronoamperometry was conducted at 1.23 V vs. RHE in 1 M NaOH under chopped illumination for more than 16 h to test the stability. All experiments were performed at ambient temperature and electrode potentials were converted to the RHE scale using E (RHE) = E (Ag/AgCl) + 0.197 V + 0.059 pH (pH = 13.6 for 1 M NaOH). E (RHE) and E (Ag/AgCl) are the converted potential versus RHE and the measured potential versus Ag/AgCl reference electrode, respectively.

Supporting Table

Table S1. Four-point DC resistivity measurements of FTO substrates treated with different annealing temperatures for 20 min.

| Temperature (°C)	No annealing	500	600	700	800
$R_{ave}(\Omega/\square)$	12.1	31.1	31.8	31.3	31.6

Supporting figures:
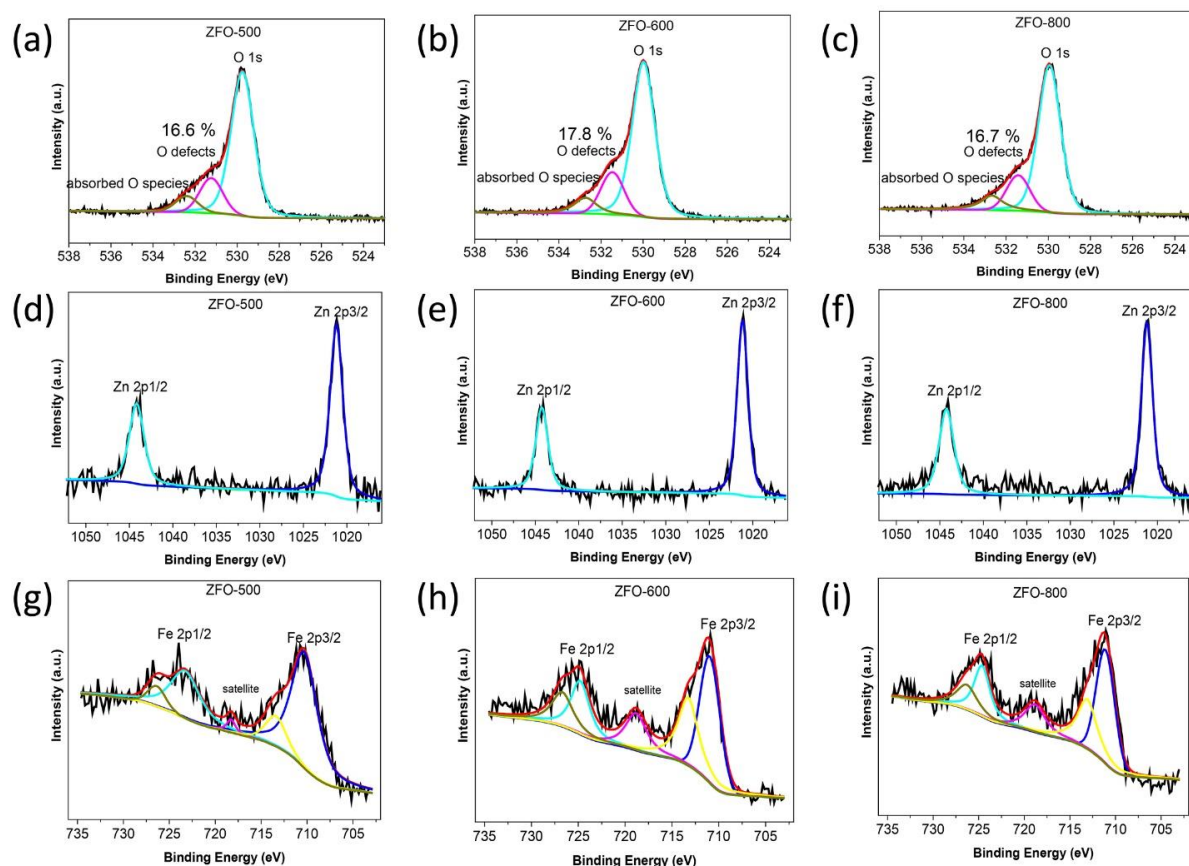
Figure S1. Detailed X-ray photoelectron spectroscopy (XPS) of the ZFO photoelectrodes (a,d,g) are ZFO-500, (b,e,h) are ZFO 600, and (c,f,i) are ZFO 800. High-resolution spectra are shown in the energy ranges of the O 1s signal (a,b,c), the Zn 2p signal (d,e,f), and the Fe 2p signal (g,h,i).
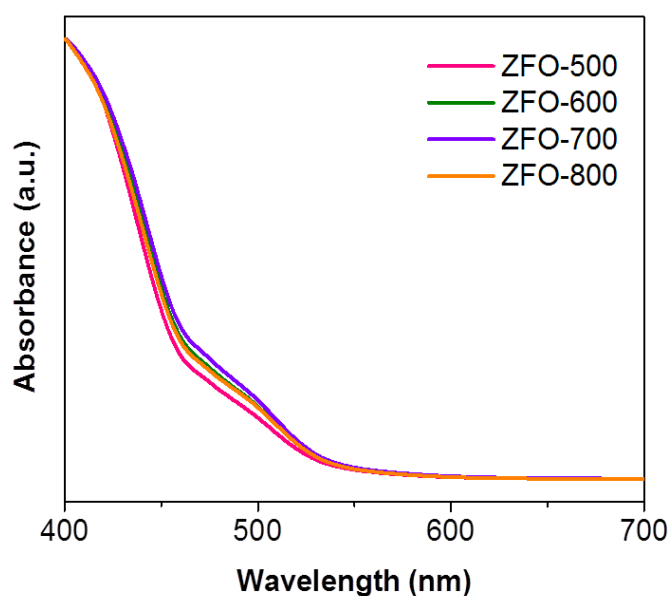

Figure S2. The UV-Vis absorption spectra of the as-prepared photoelectrodes on FTO coated glass substrates.

19
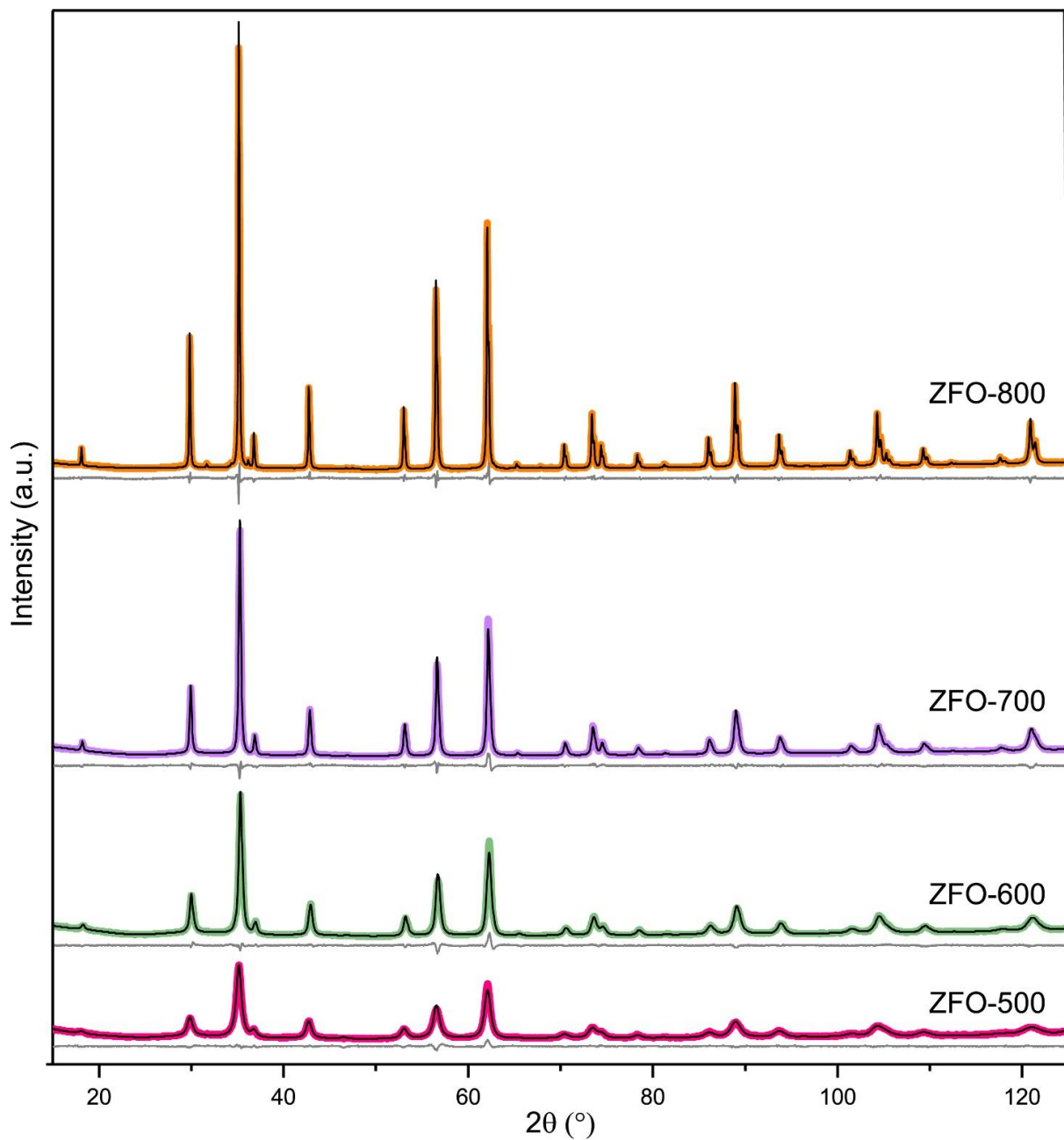
Figure S3. Powder XRD of the ZFO samples prepared at different temperatures. The colored trace is the experimental data, the superimposed black trace is the fit Rietveld refinement and the gray trace below each pattern is the residual. The agreement factors for Rietveld refinement are: (500°C) R_{wp} = 7.24 (background-corrected); (600°C) R_{wp} = 6.83; (700°C) R_{wp} = 5.64; (800°C) R_{wp} = 5.29.
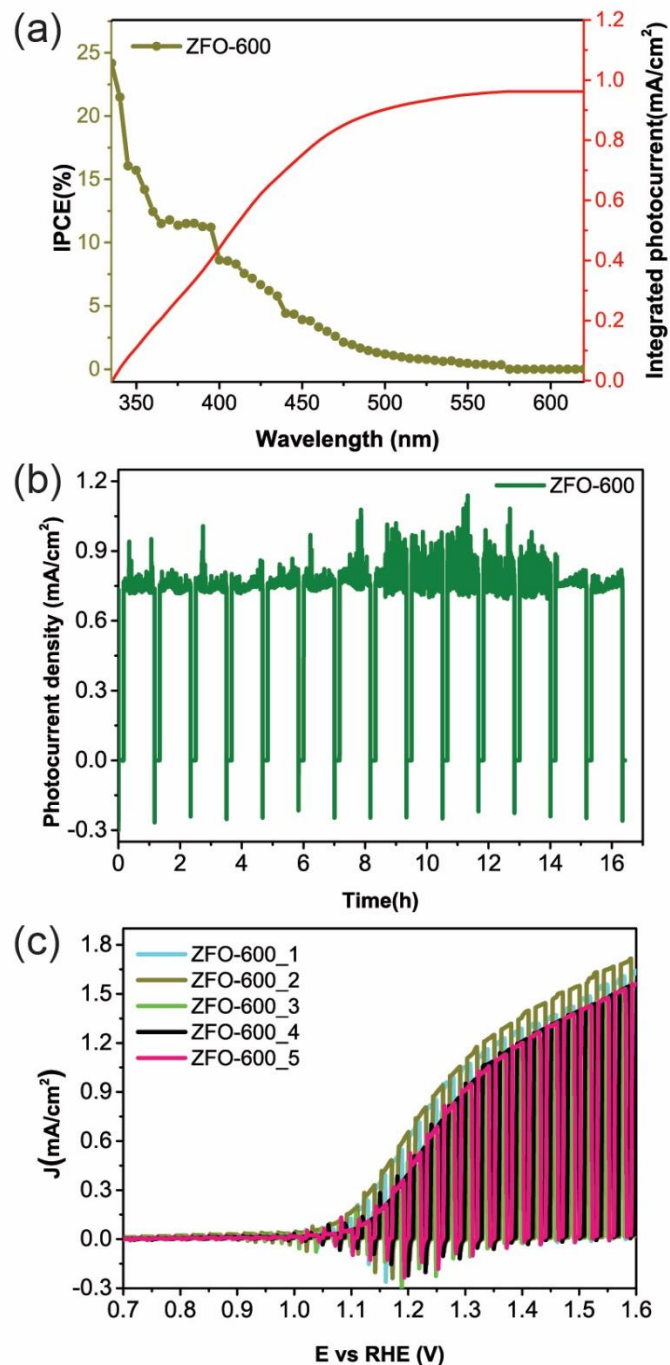
Figure S4. Additional photoelectrochemical characterization of the ZFO-600 samples. (a) IPCE in 1M NaOH at 1.23 V vs RHE as a function of illumination wavelength. The integration of the IPCE with the standard AM 1.5 G solar spectrum (100 mW cm^{-2}) is also shown. (b) The chronoamperometry of ZFO-600 at 1.23 V vs RHE under chopped illumination in 1M NaOH electrolyte for 16 hours. (c) The reproducibility of the optimized ZFO-600 conditions with the J-V curves of 5 separately-prepared ZFO-600 samples.

21
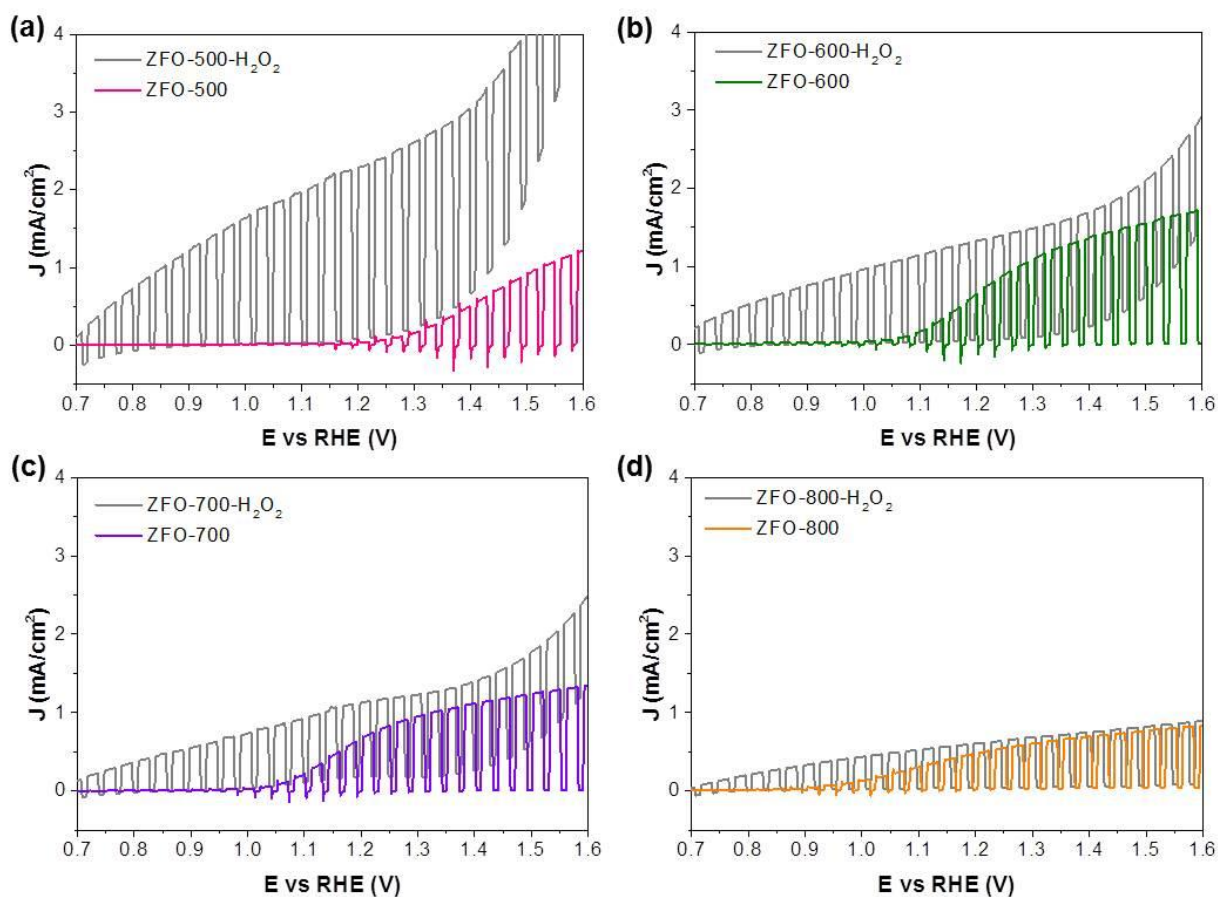
Figure S5. J-V curves under intermittent simulated solar illumination for ZFO-500(a), ZFO-600(b), ZFO-700(c) and ZFO-800(d) in 1M NaOH with and without 0.5 M H_2O_2 added as a sacrificial hole acceptor.

22
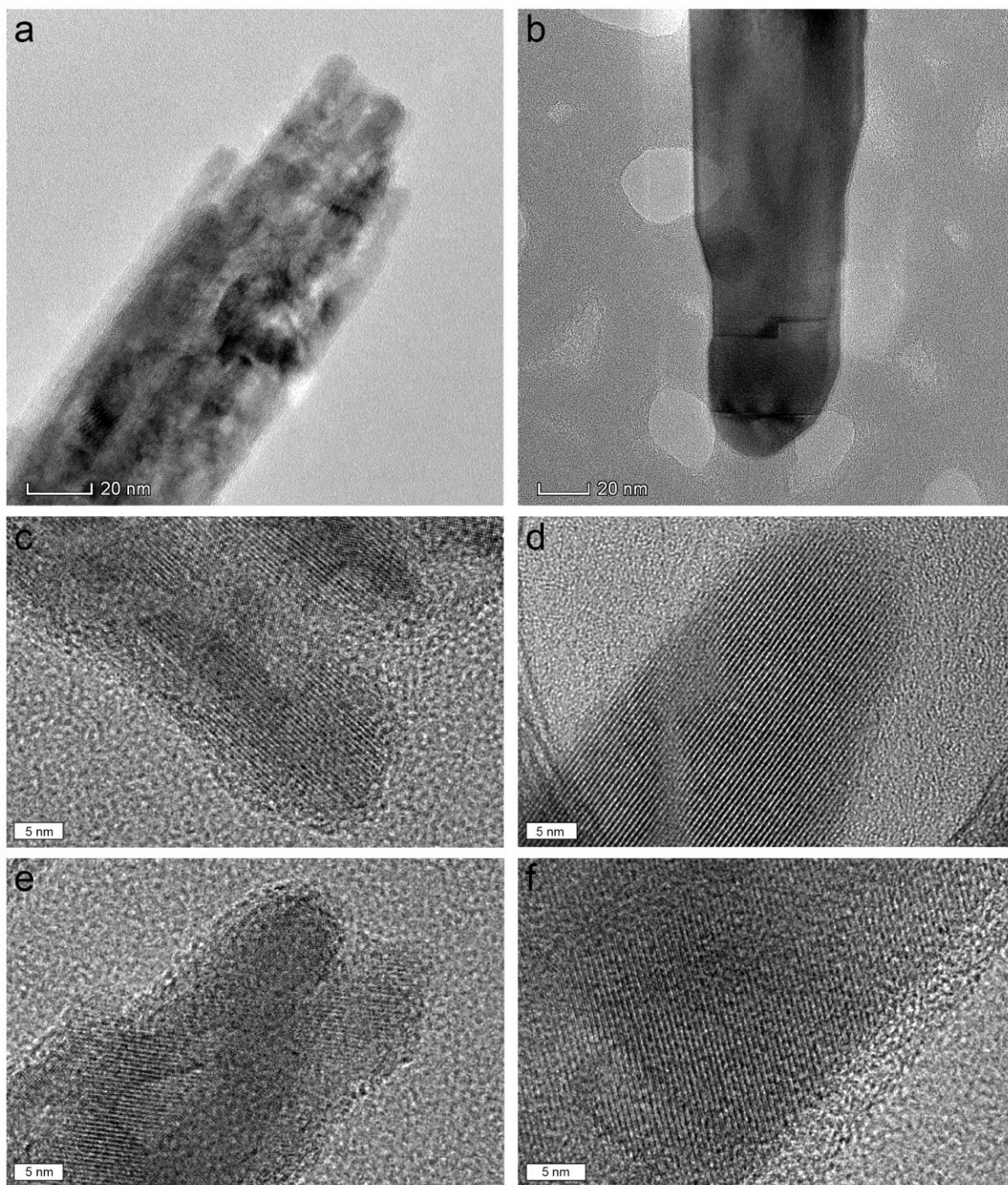
Figure S6. High resolution transmission electron microscopy images of a nanorod removed from a ZFO-500 sample (a,c,e) and a ZFO-800 sample (b,d,f).
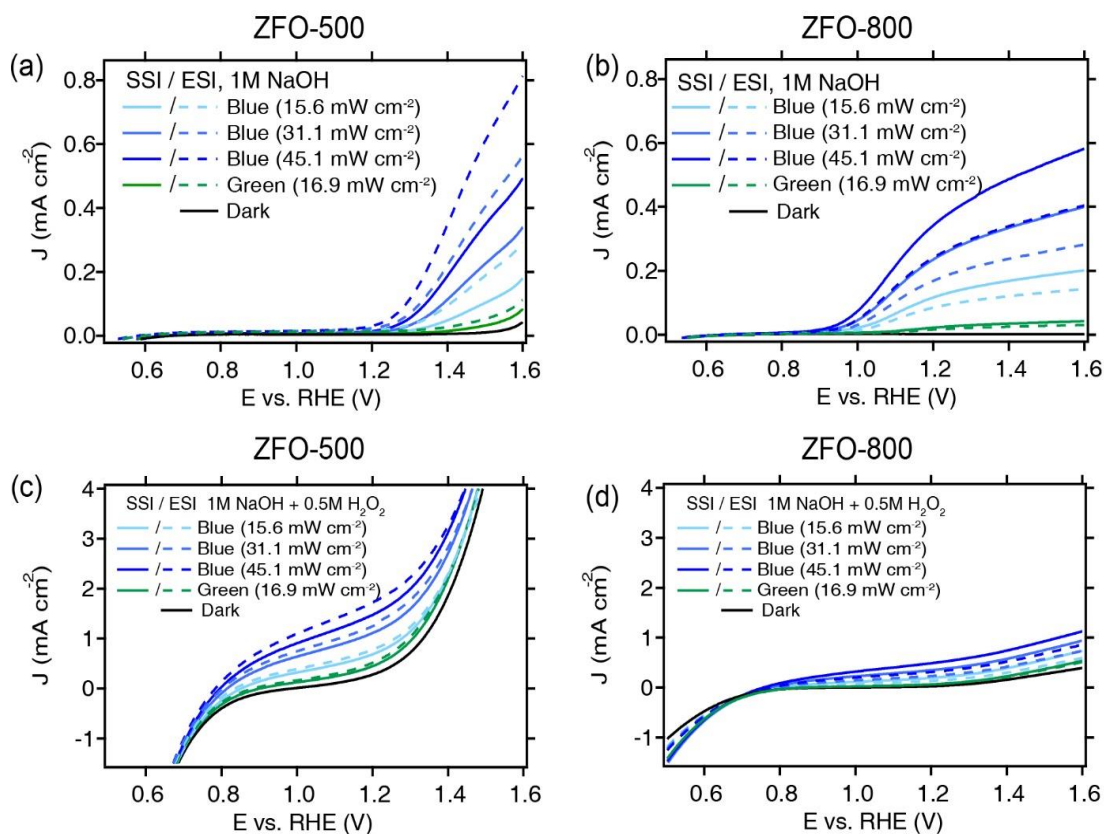
Figure S7. The effect of substrate side illumination (SSI – solid lines) and electrolyte side illumination (ESI – dashed lines) on the J-V curves of ZFO-500 (a,c) and ZFO-800 (b,d) without (a,b) and with (c,d) sacrificial holes scavenger (1 M NaOH + 0.5 M H_2O_2) and under monochromatic light (blue $\lambda = 452$ nm, green $\lambda = 525$ nm). The different light intensities under blue illumination show that the effect depend on the light intensity, and the green illuminated samples shows that the J-V curves are more similar when not zonally defining the photogenerated charge carriers, as expected.
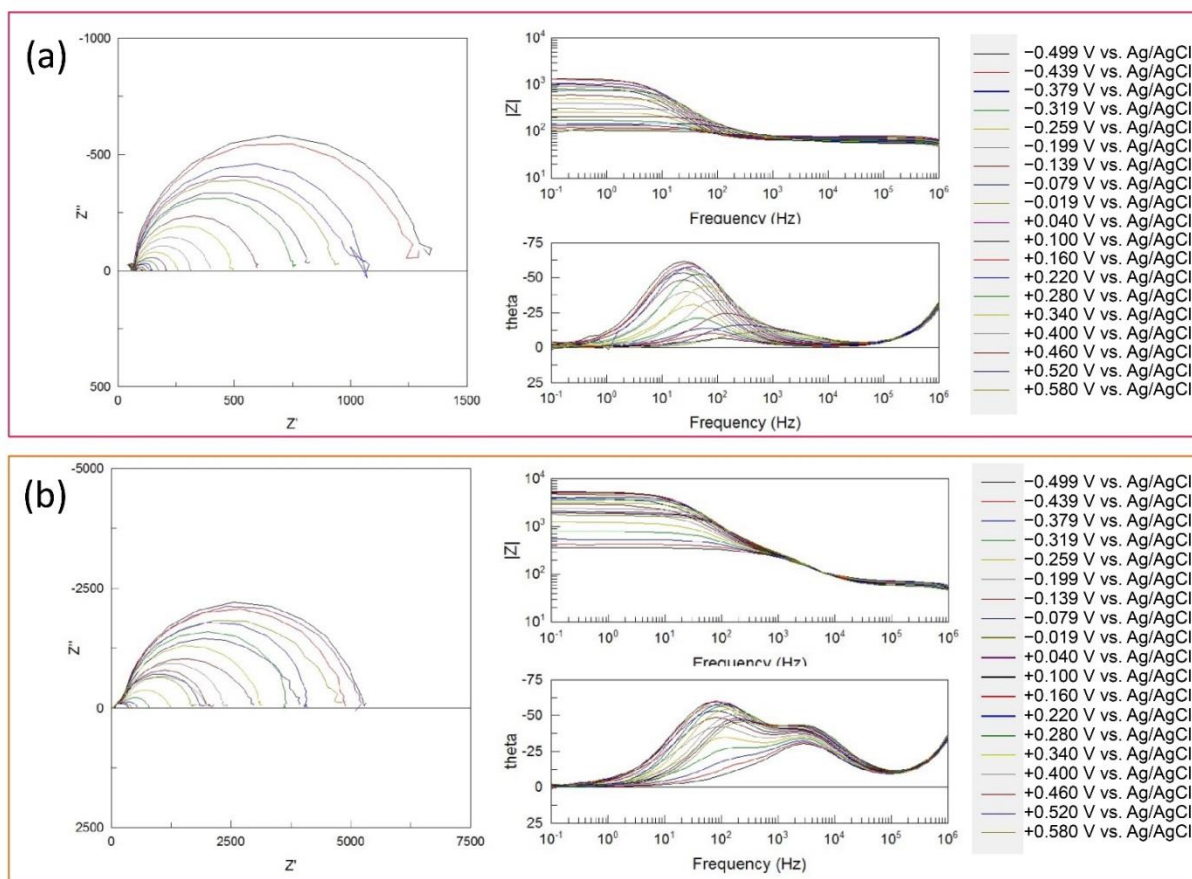
Figure S8. Electrochemical impedance spectra (Nyquist plots and bode plots) of (a) ZFO-500 and (b) ZFO-800 in 1M NaOH with 0.5 M H_2O_2 under 1 sun illumination at different applied potentials as indicated. The data were fit to an equivalent circuit model as previously described,[S4] and the semiconductor resistance was extracted for Figure 4c (main text).
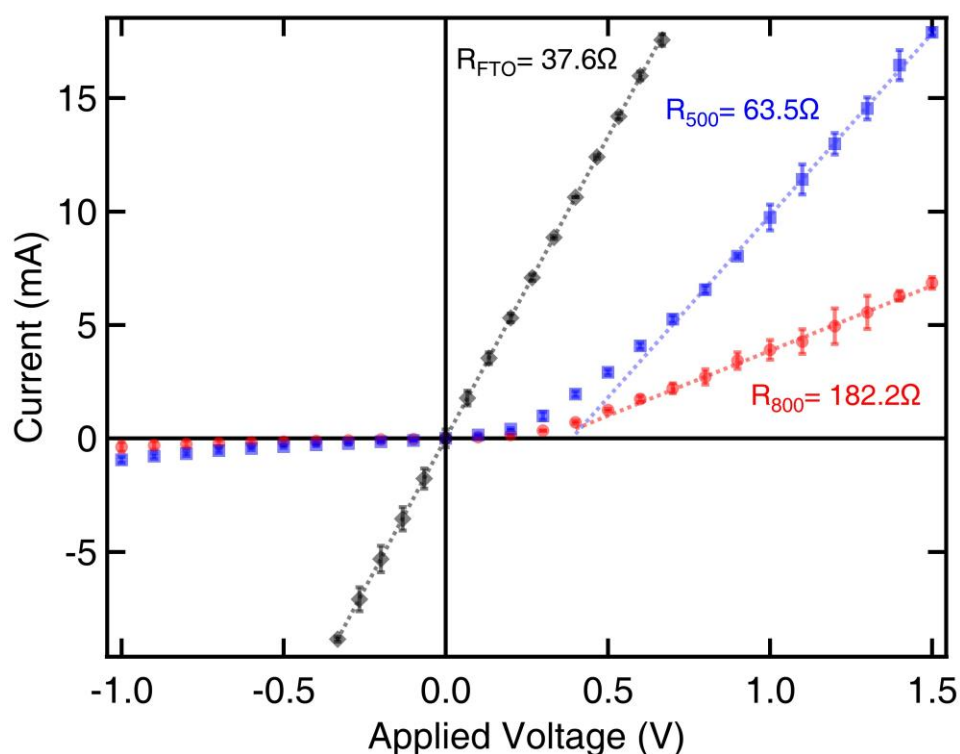
Figure S9. Conductivity measurements are shown by current-voltage curves for ZFO-500 (blue squares) and ZFO-800 (red circles) acquired in the direction perpendicular to the substrate (*i.e.* in the axial direction of the nanorods) via contact made with a eutectic Gallium–Indium as previously described.[S5] The reported data represent an average of 5 measurements performed on each sample (error bars represent standard deviation). Linear fits (dotted lines) were performed in the respective ohmic regions and gave $R^2 > 0.99$ in all cases. We note that the estimated value of the resistance of the FTO blank matches well with the four-point measurements reported in Table S1. The respective conductivity of the ZFO-500 and ZFO-800 is estimated below in calculation Note S3 and reported in Table S3.
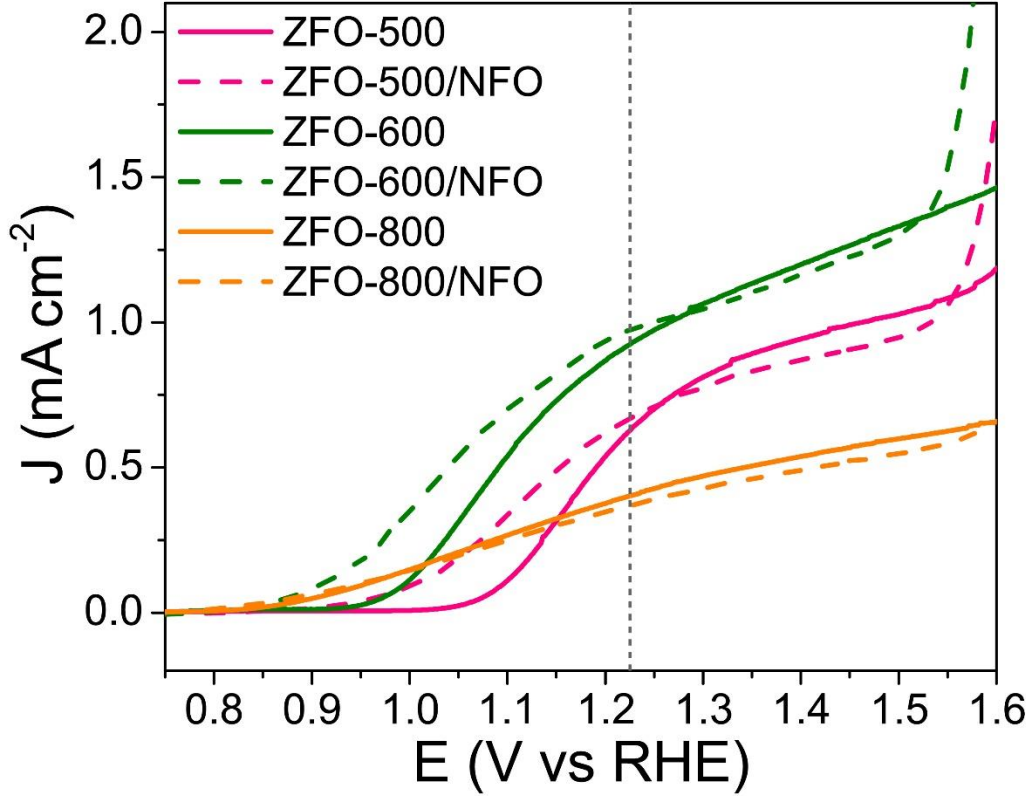
Figure S10. J-V curves of the ZFO photoelectrodes with (and without) nickel-iron-oxide (NFO) co-catalyst under illumination (Simulated AM 1.5G 100 mW cm^{-2}) in 1 M NaOH electrolyte. The vertical dashed line represents 1.23 V vs RHE.

Calculation Notes:

Note S1. Calculation of the theoretical maximum photocurrent density (J_{abs})

The maximum possible photocurrent, J_{abs}, is estimated using the standard solar spectrum and the measured absorbance of the photoelectrode as:

$$J_{abs} = q \int_{\lambda 1}^{\lambda 2} N(\lambda)_{AM1.5} \, LHE(\lambda) \, d\lambda$$

where $\quad N(\lambda)_{AM1.5} = \dfrac{\Phi(\lambda)_{AM1.5}}{E} = \dfrac{\lambda \, \Phi(\lambda)_{AM1.5}}{h \, c} \quad$ and $\quad LHE = 1 - 10^{-A(\lambda)}$

Thus we write,

$$J_{abs} = \frac{q}{hc} \int_{\lambda 1}^{\lambda 2} \Phi(\lambda)_{AM1.5} \times \lambda \times \left(1 - 10^{A(\lambda)}\right) d\lambda$$

Here $N(\lambda)_{AM1.5}$ (in units of m^{-2}s^{-1}) is the photon flux density under standard conditions (AM1.5G 100 mW cm^{-2}), $\Phi(\lambda)_{AM1.5}$ (unit of Wm^{-2}nm^{-1}) is the energy of photons from the solar simulator in unit area and unit time, E is the energy of one photon, λ (unit of nm) is the wavelength of photon, h (6.626×10^{-34} J·s) is Planck's constant, q (1.602×10^{-19} C) is the charge of one electron, LHE represents the light harvesting efficiency, $A(\lambda)$ is the measured absorbance of the photoelectrode. Specifically, for ZFO photoanodes in this work, J_{abs} was

27

calculated to be of 7.47 mA/cm^2 by integrating until 590 nm (2.1 eV, corresponding to the direct bandgap) according to the following equation:

$$J_{abs}\left(\frac{mA}{cm^2}\right) = 0.806 \times 10^{-4} \int_{300}^{590} \left(1 - 10^{A(\lambda)}\right) \Phi(\lambda)_{AM1.5} \lambda \, d\lambda$$

Note. S2 Evaluation of blue light (@452 nm) and green light (@525 nm) absorption depth

a) Measurements and calculation of absorption coefficient (α)

Accurate estimation required that the reflectance is taken into account, thus

$$I_t = (I_0 - I_r) \times e^{-\alpha h}$$

$$T(\%) = \left(100 - R(\%)\right) \times e^{-\alpha h}$$

So then

$$\alpha = -\frac{1}{h}\ln(\frac{T(\%)}{100 - R(\%)})$$

here h is the thickness of the zinc ferrite film, I_0, I_t and I_r is the intensity of the incident light transmission, and reflection light, respectively. T and R represent the transmittance and reflectance, respectively, which were measured by UV-vis-NIR UV-3600 (Shimadzu) spectrophotometer. The following figure is the as-measured absorption coefficients for ZFO-500 and ZFO-800.
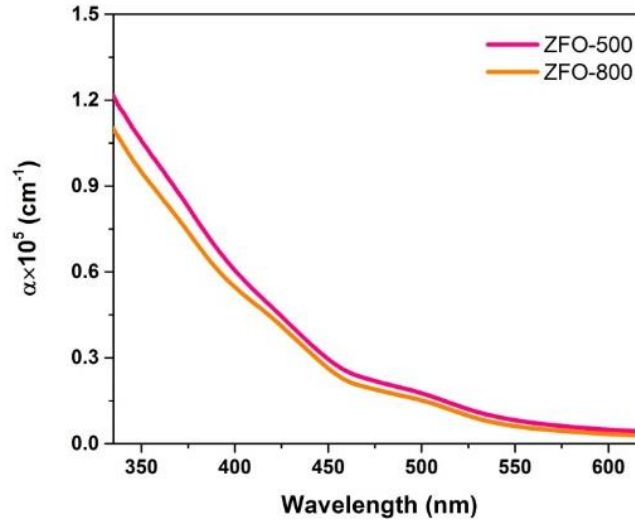
Figure S11. Estimated Absoption coefficient as a function of photon wavelength for select ZFO photoanodes.

b) The correction of absorption coefficient (α) due to the nanostructure

The above-estimated absorption coefficients are based on the assumption where the measured sample is compact flat film. Since our films are nanorod arrays, the absorption coefficient should be corrected by estimating the void percentage of the nanostructured film. The average number (N) of nanorods in area of 400 nm × 400 nm are counted in SEM top-view images as

shown in Fig.1 (main text). Then, the total volume occupied by the nanorods is estimated by the following formula:

$$V_n = N \cdot \pi r^2 h$$

In which, r is the average radius of nanorods and h is the thickness nanostructured film. The hypothetical absorption volume of compact film is $V_c = 400\ nm \cdot 400\ nm \cdot h$

Thus,

$$P_{Void} = 1 - \frac{V_n}{V_c}$$

The corrected absorption coefficient is then

$$\alpha_c = \frac{\alpha_m}{1 - P_{Void}}$$

Therefore, the absorption depth at wavelength of λ

$$d_{abs}(\lambda) = \frac{1}{\alpha_c(\lambda)}$$

The estimated results are listed in the following table:

Table S2: Optical parameters and the estimated absoption depth, d_{abs}, for the ZFO-500 and ZFO-800 samples.

sample	N	r /nm	h /nm	P_{Viod}	α_m(@452nm) /cm^{-1}	d_{abs}(@452 nm)/nm	α_m(@525nm) /cm^{-1}	d_{abs}(@525 nm)/nm
ZFO-500	51	21	500	0.44	0.286×10^5	195	0.120×10^5	465
ZFO-800	40	24	500	0.45	0.253×10^5	216	0.098×10^5	559

Note. S3 Conductivity measurements

Calculations of the electrical conductivity σ:

The electrical conductivity is given by: $\sigma = \frac{h}{R_{corr}\ A_{xs}\ (1-P_{Void})}$

With R_{corr} as the corrected measured resistance (subtracting the substrate resistance,), A_{xs} the cross-sectional area (the area of the eutectic Gallium–Indium contact), P_{Void} is the void fraction of the nanorod arrays and h the height of the nanorods. The results are tabulated below.

Table S3: Conductivity measurements

sample	R^a / Ω	R_{corr} / Ω	h /nm	P_{Viod}	A_{xs} / mm^2	σ / μS/cm
ZFO-500	63.5	25.9	500	0.44	3.87	89.1
ZFO-800	182.2	144.6	500	0.45	5.09	12.4

[a] as measured in Figure S9

Supporting references.

[S1] L. Vayssieres, N. Beermann, S.-E. Lindquist and A. Hagfeldt, *Chem. Mater.*, **2001**, *13*, 233–235.

[S2] N. Guijarro, P. Bornoz, M. Prévot, X. Yu, X. Zhu, M. Johnson, X. Jeanbourquin, F. L. Formal and K. Sivula, *Sustain. Energy Fuels*, **2018**, *2*, 103–117.

[S3] A. A. Coelho, *J. Appl. Crystallogr.*, **2000**, *33*, 899–908.

[S4] F. Le Formal, S. R. Pendlebury, M. Cornuz, S. D. Tilley, M. Grätzel and J. R. Durrant, *J. Am. Chem. Soc.*, **2014**, *136*, 2564–2574.

[S5] E. A. Weiss, V. J. Porter, R. C. Chiechi, S. M. Geyer, D. C. Bell, M. G. Bawendi, G. M. Whitesides, *J. Am. Chem. Soc.* **2008**, *130*, 83.